

# GMG: A Video Prediction Method Based on Global Focus and Motion Guided

Yuhao Du<sup>1</sup> Hui Liu<sup>2</sup> Haoxiang Peng<sup>2</sup> Xinyuan Cheng<sup>3</sup> Chenrong Wu<sup>4</sup> Jiankai Zhang<sup>1,\*</sup>

<sup>1</sup>College of Atmospheric Sciences, Lanzhou University, Lanzhou, China

<sup>2</sup>College of Computer and Mathematics, Central South University of Forestry and Technology, Changsha, China

<sup>3</sup>Center for Language and Information Processing, University of Munich (LMU), Munich, Germany

<sup>4</sup>Department of Computer Science, University of Manchester, Manchester, UK

{duyh2024, jkzhang}@lzu.edu.cn, {T20030970, 20235223}@csuft.edu.cn,  
Xinyuan.Cheng@campus.lmu.de, chengrong.wu@student.Manchester.ac.uk

**Abstract**—Recent years, weather forecasting has gained significant attention. However, accurately predicting weather remains a challenge due to the rapid variability of meteorological data and potential teleconnections. Current spatiotemporal forecasting models primarily rely on convolution operations or sliding windows for feature extraction. These methods are limited by the size of the convolutional kernel or sliding window, making it difficult to capture and identify potential teleconnection features in meteorological data. Additionally, weather data often involve non-rigid bodies, whose motion processes are accompanied by unpredictable deformations, further complicating the forecasting task. In this paper, we propose the GMG model to address these two core challenges. The Global Focus Module, a key component of our model, enhances the global receptive field, while the Motion Guided Module adapts to the growth or dissipation processes of non-rigid bodies. Through extensive evaluations, our method demonstrates competitive performance across various complex tasks, providing a novel approach to improving the predictive accuracy of complex spatiotemporal data.

**Index Terms**—Spatio-temporal, Video Prediction, Motion Guided, Global receptive field.

## I. INTRODUCTION

In recent years, spatiotemporal prediction has garnered unprecedented attention due to the growing demand for prediction tasks across various domains, particularly in weather forecasting [1], [2] and traffic prediction [3], [4]. Accurate predictions can bring significant social and economic value. Currently, spatiotemporal prediction models can be categorized into four main types: RNN, CNN, CNN-RNN, and ViT.

RNN models primarily rely on stacking basic predictive units to transmit information in both depth and breadth. The advantage of RNN lies in its ability to capture long-term temporal features, though these models generally involve a large number of parameters. Classic RNN models include PredRNN [4], PredRNN++ [5], MIM [6], MotionRNN [7], PredRNN-V2 [8], and VMRNN [9]. These models improve prediction performance by optimizing the organization and transmission of information flows or parameter handling.

\* Corresponding author

This research was supported by the National Natural Science Foundation of China (U2442211), Scientific Research Fund of Hunan Provincial Education Department (24C0128). The computations in this research was supported by Supercomputing Center of Lanzhou University. The source code will be released at <https://github.com/duyhlzu/GMG>.

CNN models focus on capturing multiscale features through techniques such as multiscale convolution stacking, upsampling, and skip connections. The strength of CNN models lies in their simplicity, allowing them to capture multiscale features efficiently, although they often struggle to capture long-term temporal features. Notable CNN models include PredCNN [10], SimVP [11], and TAU [12], which have demonstrated excellent performance and interpretability using streamlined predictive frameworks, offering diverse solutions for spatiotemporal sequence prediction.

Hybrid CNN-RNN models enhance the predictive capability of RNNs by preprocessing input data and extracting multiscale features using CNNs. Models like E3D-LSTM [13], CrevNet [14], and PhyDNet [15] achieve accurate and efficient predictions through different CNN encoders for effective feature extraction.

ViT primarily utilizes the Transformer architecture, which has gained popularity in recent years, leveraging the attention mechanism to capture image features. SwinLSTM [16], SimVP-ViT [17], and PredFormer [18] are built on Vision Transformer [19] or Swin Transformer [20] backbones. As an emerging approach, ViT models have been proven to possess strong predictive capabilities. However, due to the high computational complexity of attention mechanisms, they typically require more training resources.

Meteorological data prediction holds significant research value due to its timeliness and immense societal impact. However, spatiotemporal data often exhibit complex non-stationary processes with rapid short-term variations, making prediction tasks highly challenging. This paper focuses on two core issues (Figure 1): deformation caused by object motion and potential long-range correlations.

Taking precipitation data as an example, rain clouds not only shift in a specific direction but also undergo overall deformation. Moreover, the dissipation and growth of clouds over time are particularly difficult to predict accurately. Similarly, in real life, a traffic jam on one street may impact another distant street. In meteorological data, analogous phenomena exist where climate anomalies exhibit correlations over long distances. However, the complexity and unpredictability of such long-range correlations significantly limit prediction ac-

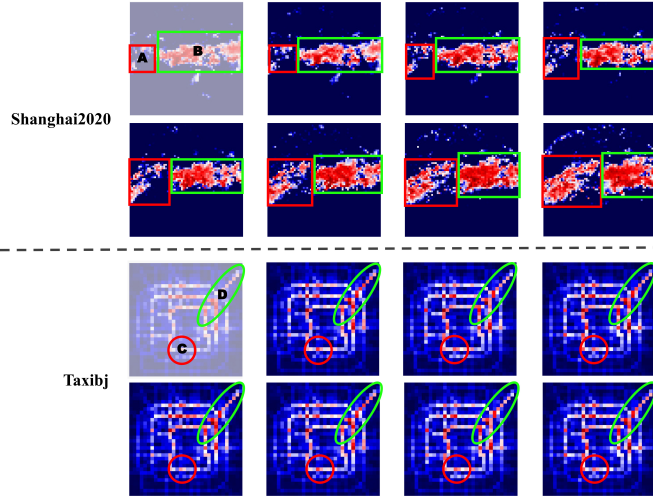


Fig. 1. The two main real-world challenges addressed in this paper. Position and shape changes of rainfall regions over time: For example, in region B, while moving eastward, the north-south extent of the rainfall gradually expands, adding complexity to prediction tasks. Long-range correlations: In real-life scenarios, a traffic jam in region C may impact traffic in another part of the city, such as region D. These long-range correlations are often difficult to capture, limiting the accuracy of predictions for such data.

curacy.

Previous studies have developed models that decouple motion patterns to better predict object motion. MotionRNN, for instance, decomposes motion into transient variation and trending momentum to model object motion dynamics. MAU [21] separately trains augmented motion information (AMI) and current spatial state to capture reliable inter-frame motion information. MMVP [22] constructs an appearance-independent motion matrix to decouple motion and appearance information, inferring future object motion from image frames while maintaining appearance consistency across frames. These studies provide valuable theoretical foundations. Building on these, we propose a Motion Guided Module (MGM) to better predict deformations arising during object motion. Extending MotionRNN’s displacement decomposition framework, we introduce a deformation pattern regulated by a balance factor  $\alpha$  and a decay factor  $\beta$  to simulate this non-stationary process effectively.

Despite the advances achieved by current methods through enhanced information flow mechanisms, multiscale convolution stacking, or sliding-window strategies to broaden the model’s global perspective, a critical issue remains: whether based on convolutions or sliding windows, the receptive field of these approaches is inherently limited. This limitation makes it challenging for models to fully capture and generalize global features when processing spatiotemporal data with potential long-range correlations. To address this, we propose a Global Focus Module (GFM) that enhances the model’s global perspective by extracting global features from the input image  $X$  and integrating them with the hidden state  $H$ .

The proposed GMG predictive model consists of four main components: SpatioTemporal ConvLSTM (ST-ConvLSTM),

Motion Guided Module (MGM), Self-Attention Memory, and Global Focus Module (GFM). We aim to offer a general solution for video prediction, particularly for meteorological data, and provide a novel approach to achieving accurate meteorological forecasting. The main contributions of this paper are summarized as follows:

- We propose a more comprehensive object motion decoupling method, the **Motion Guided Module (MGM)**, which captures non-elastic deformation characteristics by introducing a **balance factor** and a **decay factor**.
- We develop a **Global Focus Module (GFM)** to address the limitations of convolutional receptive field size, enabling the model to capture potential long-range feature correlations.
- By integrating MGM and GFM, we propose the **GMG video prediction framework**. Extensive experiments on five different types of datasets demonstrate that GMG achieves state-of-the-art performance, providing an innovative solution for video prediction.

## II. RELATED WORK

Over the past decade, spatiotemporal prediction using recurrent structures has originated from ConvLSTM, a simple yet effective framework that remains widely used today. Following this, numerous RNN-based models have been proposed. PredRNN [4] introduced ST-ConvLSTM, which added a Spatiotemporal Memory module parallel to the cell state in ConvLSTM and organized a cross-layer information flow. This design allowed the model’s final output to comprehensively capture hierarchical spatiotemporal features. Building upon PredRNN, PredRNN++ [5] regulated the sequence of spatiotemporal memory and cell states, leading to the introduction of Causal LSTM. Additionally, the authors proposed the Gradient Highway Unit, enabling rapid transmission of hidden states between adjacent basic units to mitigate gradient vanishing along the temporal dimension.

To further enhance the prediction capability for non-stationary data, MIM introduced a differential computation between the hidden states of adjacent recurrent nodes, effectively reducing the higher-order non-stationarity in spatiotemporal data. MIM also reorganized the hidden state transmission mechanism, enabling diagonal transmission of information. This allowed basic units to fully utilize the differential pattern. MotionRNN [7] extended PredRNN by decomposing hidden states into two motion states: Transient Variation ( $F$ ) and Trending Momentum ( $D$ ), trained using GRU. This approach achieved accurate predictions for moving objects and demonstrated strong performance on radar echo data. SwinLSTM [16], inspired by Swin Transformer, segmented images into patches as tokens for input while retaining the fundamental RNN framework, introducing a new perspective for RNN-based improvements. Similarly, VMRRN [9] combined Vision Mamba with RNN. Like SwinLSTM, it processed image tokens but employed a selective state-space model for input handling.

Notably, the GMG proposed in this paper is also implemented based on the fundamental RNN architecture as a basic predictive unit. Furthermore, the core module of GMG, the Global Focus Module, is a flexible and independent component. This design allows it to integrate seamlessly with the aforementioned RNN-based predictive models without structural modifications. Unlike previous prediction methods, we emphasize expanding the model's global perspective and designing a learning module specifically for handling shape variations in moving objects. Our approach provides a novel solution for video prediction, particularly for meteorological data with complex dynamic processes.

### III. METHODS

#### A. Overall Architecture

The overall architecture of GMG is presented on the left side of Fig. 2. The input image  $X$  is processed through ST-ConvLSTM to update the hidden state  $H_t$ . Subsequently,  $H_t$  is fed into the Global Focus Module (GFM), where it is fused with global features to produce  $H_t^g$ , enabling the model to perceive global characteristics of the input data. The primary role of SAM [24] is to integrate  $H_t^g$  with the spatiotemporal memory  $M_t$  to capture spatial contextual information, thereby enhancing the model's ability to maintain long-term feature dependencies. Finally,  $\hat{H}_t^g$  is input into the Motion Guided Module (MGM), which regulates the model's motion state learning ability through two state factors,  $\alpha$  and  $\beta$ . GMG retains the cross-layer transmission of spatiotemporal memory and the Gradient Highway Unit [5], ensuring effective utilization of various types of valuable information.

#### B. Global Focus Module

In Section 1, we discuss the challenges that existing methods face in capturing long-range correlations. In this section, we introduce a global correction approach: the Global Focus Module (Fig. 2, right). In the actual training process, features are typically not extracted from the entire image but are processed by dividing the image into patches or using a sliding window approach. Additionally, due to the limitation of the kernel size, the receptive field of the model is restricted, which leads to the model's inability to capture potential correlations between distant regions in the image. Therefore, we propose a visual focusing approach. After processing the local features, we revisit the entire image's features and inform the model of the important global region correlations to capture the potential long-range dependencies.

First, we apply Adaptive Average Pooling (AAP) to extract the **Global Features** ( $G_F \in \mathbb{R}^{T \times C \times H \times W}$ ) from the input image:

$$G_F = \text{AAP}(\text{ReLU}(\text{Conv2d}(X_t))). \quad (1)$$

Then, a linear fully connected layer is used to map the  $G_F$  to a specified dimensional space:

$$X_t^g = \text{ReLU}(\text{Linear}(G_F)). \quad (2)$$

We also design a gate mechanism to control the degree of fusion between the global features and the hidden state:

$$\mathcal{G} = \text{Sigmoid}(\text{Conv2d}(\text{Concat}[H_t, X_t^g])), \quad (3)$$

$$H_t^g = H_t \circ \mathcal{G} + X_t^g \circ (1 - \mathcal{G}). \quad (4)$$

Where,  $X_t^g, H_t \in \mathbb{R}^{T \times C \times H \times W}$ ,  $\circ$  denote the Hadamard product. To ensure that the updated hidden state includes more global information across different scales, we apply a multi-scale focus method:

$$g_t = \text{MultiScaleConv}_{(1,3,5)}(X_t), \quad (5)$$

$$H_t^g = H_t^g \circ g_t. \quad (6)$$

Where  $\text{MultiScaleConv}_{(*)}$  represents feature extraction using different-sized convolution kernels, and the final output is the sum of all feature maps,  $g_t \in \mathbb{R}^{T \times C}$ . Then,  $g_t$  will be broadcasted to the same shape as  $H_t^g \in \mathbb{R}^{T \times C \times H \times W}$ . We refer to the operation in Eq.(6) as "Feature Focus".

#### C. Motion Guided Module

Inspired by the motion decomposition in MotionGRU [7], we propose a decomposition model based on motion evolution. This model divides the spatial movement of objects into transient variations  $\mathcal{F}$  and trending momentum  $\mathcal{D}$ .  $\mathcal{F}, \mathcal{D} \in \mathbb{R}^{T \times 2k^2 \times \frac{H}{2} \times \frac{W}{2}}$ ,  $k$  is filter size. Additionally, it generalizes non-displacement changes of objects as the cumulative effects of two physical processes: collision and dissipation. To effectively capture the features of object deformation, we introduce a balance factor  $\alpha$  and a decay factor  $\beta$ , which illustrated on the right side of Fig. 2.

First, the MGM processes the transient variations  $F$  and trending momentum  $D$  using GRU:

$$u_t = \sigma(\text{Conv2d}(\text{Concat}([\hat{H}_t^g, \mathcal{F}_{t-1}]))), \quad (7)$$

$$r_t = \sigma(\text{Conv2d}(\text{Concat}([\hat{H}_t^g, \mathcal{F}_{t-1}]))), \quad (8)$$

$$z_t = \tanh(\text{Conv2d}(\text{Concat}([\hat{H}_t^g, \mathcal{F}_{t-1} \circ r_t]))), \quad (9)$$

where  $u_t$  is the Update Gate,  $r_t$  is the Reset Gate, and  $z_t$  is the reset feature of the current moment. In this equation,  $\hat{H}_t^g$  will be processed by a stride-2 convolution into a shape of :  $\hat{H}_t^g \in \mathbb{R}^{T \times \frac{C}{4} \times \frac{H}{2} \times \frac{W}{2}}$ .

Then, the gate mechanism updates  $\mathcal{F}'_{t-1}$  as follows:

$$\mathcal{F}'_{t-1} = \mathcal{F}_{t-1} \circ (1 - u_t) + z_t \circ u_t. \quad (10)$$

Unlike the Global Focus Module, we only use adaptive average pooling to extract dynamic features from the hidden state  $\hat{H}_t^g$ :

$$G_T = \text{AAP}(\hat{H}_t^g). \quad (11)$$

Based on this dynamic feature, we calculate the dynamic balance factor  $\alpha_d$  and dynamic decay factor  $\beta_d$ :

$$\alpha_d, \beta_d = \sigma(\text{Linear}(G_T)). \quad (12)$$

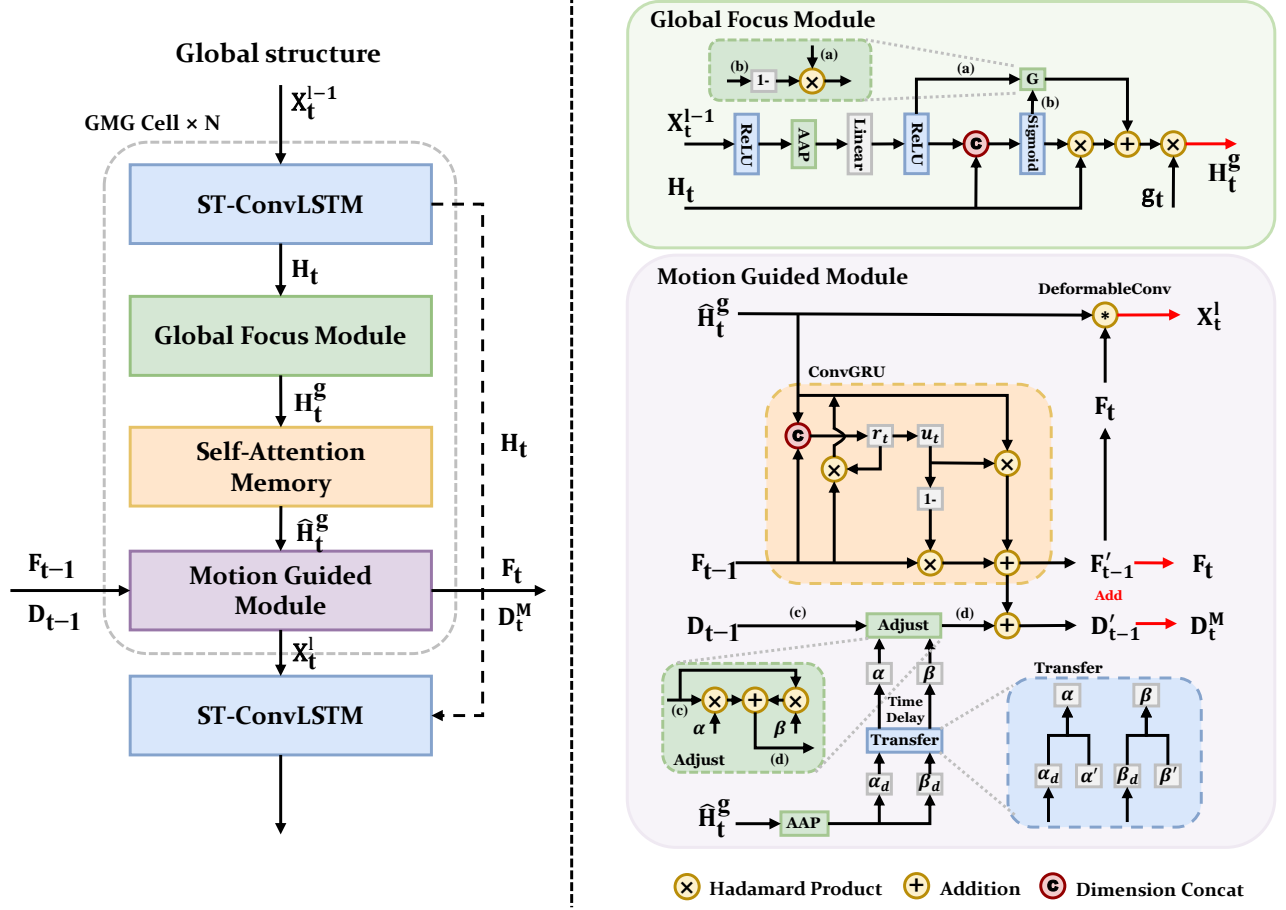


Fig. 2. The overall structure of GMG (left) and the two main modules proposed in this paper (right) are illustrated. A standard GMG unit consists of four modules: ST-ConvLSTM, Global Focus Module, Self-Attention Memory, and Motion Guided Module. In this study, each time step is composed of four stacked GMG units. The temporal memory  $M$  from the fourth layer at time  $t$  is transferred to the first layer at time  $t + 1$ , ensuring that the model captures long-term temporal dynamics effectively. The "Time Delay" in the figure refers to the operation corresponding to Eq.(15) in the text.

Next, we balance the dynamics and the default  $\alpha$  and  $\beta$ :

$$\alpha = \mathcal{T}(\alpha_d, \alpha'), \quad (13)$$

$$\beta = \mathcal{T}(\beta_d, \beta'), \quad (14)$$

where,  $\alpha'$  and  $\beta'$  are the initial parameters, respectively.  $\mathcal{T}$  is the transfer function. In this paper, the transfer function is used to fuse the values of  $\alpha$  and  $\beta$  by taking the average of the two inputs.

We also introduce an exponential decay mechanism:

$$D_e = \exp(-\beta \cdot \text{TimeSteps}), \quad (15)$$

where  $\text{TimeSteps}$  is a tensor with the same time steps as  $\mathcal{D}$ ,  $\text{TimeSteps} \in \mathbb{R}^{T \times 1 \times 1 \times 1}$ . This formula is used to simulate the effect of exponential decay, meaning that the further in time, the smaller the weight.

Object deformation can be summarized as the simultaneous action of growth and decay, so we adjust the motion trend based on the growth and decay processes:

$$\mathcal{D}'_{t-1} = D_e \cdot \mathcal{D}_{t-1} + \alpha \cdot \alpha_d \cdot \mathcal{D}_{t-1}. \quad (16)$$

According to the physical scale, the motion trend is accumulated by the transient variations:

$$\mathcal{D}_t^M = 0.5\mathcal{D}'_{t-1} + 0.5\mathcal{F}_{t-1}, \quad (17)$$

$$\mathcal{F}_t = \mathcal{D}_t^M + \mathcal{F}_{t-1}. \quad (18)$$

Finally, the transient variations are applied to the input features:

$$X_t^l = \text{DeformableConv}(\hat{H}_t^g, \mathcal{F}_t). \quad (19)$$

We use `DeformableConv` [25] to better adapt the motion variations. In addition, we propose two GMG variants to adapt to different tasks (GMG-s, GMG-m, refer to Fig. 3). To accommodate large-sample datasets, a simplified GFM is provided to reduce computational complexity:

$$G_F = \text{Conv2d}(X_t), \quad (20)$$

$$H_t^g = H_t^g \circ G_F. \quad (21)$$



The model that employs GFM-simpler is referred to as **GMG-s**. Additionally, to accommodate small-scale feature data, we omit the SAM module while retaining the GFM and other components, and this model is referred to as **GMG-m**. The base model introduced in Fig. 2 is named **GMG-L**.

#### D. Overall structure for GMG

The overall structure of the GMG model can be summarized as follows:

$$H_t, C_t, M_t = \text{ST-ConvLSTM}(X_t^{l-1}, H_{t-1}, C_{t-1}, M_{t-1}) \quad (22)$$

$$H_t^g = \text{GFM}(X_t^{l-1}, H_t) \quad (23)$$

$$\hat{H}_t^g, \hat{M}_t = \text{SAM}(H_t^g, M_t) \quad (24)$$

$$X_t^l, \mathcal{F}_t, \mathcal{D}_t^M = \text{MGM}(\hat{H}_t^g, \mathcal{F}_{t-1}, \mathcal{D}_{t-1}) \quad (25)$$

Here, GFM, SAM, and MGM correspond to the Global Focus Module, Self-Attention Memory, and Motion Guided Module, respectively. Additionally, ST-ConvLSTM can be summarized as:

$$f_t = \sigma(W_{xf} * X_t + W_{hf} * H_{t-1} + b_f) \quad (26)$$

$$i_t = \sigma(W_{xi} * X_t + W_{hi} * H_{t-1} + b_i) \quad (27)$$

$$\hat{C}_t = \tanh(W_{xc} * X_t + W_{hc} * H_{t-1} + b_c) \quad (28)$$

$$C_t = f_t \circ C_{t-1} + i_t \circ \hat{C}_t \quad (29)$$

$$f'_t = \sigma(W_{xf'} * X_t + W_{hf'} * M_{t-1} + b'_f) \quad (30)$$

$$i'_t = \sigma(W_{xi'} * X_t + W_{hi'} * \hat{M}_{t-1} + b'_i) \quad (31)$$

$$\hat{C}'_t = \tanh(W_{xc'} * X_t + W_{hc'} * M_{t-1} + b'_c) \quad (32)$$

$$M_t = f'_t \circ \hat{M}_{t-1} + i'_t \circ \hat{C}'_t \quad (33)$$

$$o_t = \sigma(W_{xo} * X_t + W_{ho} * \hat{H}_{t-1} + W_{co} * C_t + W_{mo} * M_t + b_o) \quad (34)$$

$$H_t = o_t \circ \tanh(W_{1 \times 1} * [C_t, M_t]) \quad (35)$$

where,  $*$  and  $\circ$  denote the convolution operator and the Hadamard product.

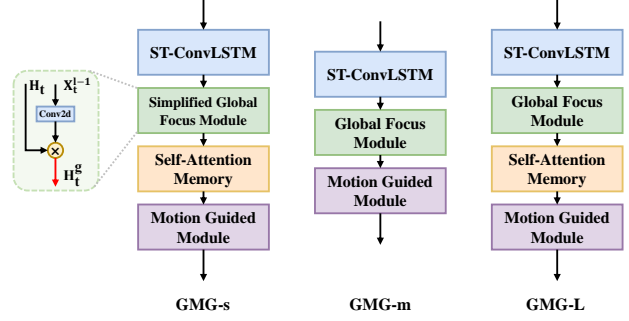


Fig. 3. Diagram of GMG and Its Variants' Architecture

## IV. EXPERIMENTS

### A. Datasets and Metrics

In this paper, we conduct experiments on five datasets: **CIKM2017** [26], **Shanghai2020** [27], **Taxibj** [28], **WeatherBench** [29] and **Moving MNIST** [31].

**CIKM2017**: This dataset, provided by the Shenzhen Meteorological Bureau, contains desensitized radar data with radar images at four altitudes. Each image has a resolution of  $101 \times 101$  square kilometers. The data is recorded at 6-minute intervals, covering 15 time steps (1.5 hours). In this study, we select 10,000 rainfall samples at the 0.5 km altitude. For each sample, the first 5 frames are used as input, and the subsequent 10 frames are predicted. The image resolution is reshaped to  $64 \times 64$ . The dataset is divided into training and validation sets with a 9:1 ratio.

**Shanghai2020**: This dataset, published by the Shanghai Central Meteorological Observatory (SCMO) in 2020, records historical precipitation events in the Yangtze River Delta region over several years. Each sample consists of 20 consecutive radar echo frames spanning 3 hours, with the first 10 frames recorded at 6-minute intervals (as input) and the last 10 frames at 12-minute intervals (as prediction). A total of 9,000 samples are used for training and 1,000 for validation. The images are reshaped to  $64 \times 64$ .

**Taxibj**: This dataset records traffic flow trajectories in Beijing, showing the inflow and outflow in each pixel of the regions using two channels. The training set contains 19,627 sample clips, and the test set contains 1,334 clips. Both training and test data have dimensions of  $2 \times 32 \times 32$ . The model learns to predict the next 4 frames based on the previous 4 frames.

**WeatherBench**: For this study, we select global temperature data (T2m) from WeatherBench, which includes 52,559 training samples and 17,495 testing samples. The image size is  $32 \times 64$ , and both input and prediction sequences consist of 12 frames with a 30-minute time interval.

**Moving MNIST**: This is one of the most popular datasets in the field of video prediction, consisting of two moving handwritten digits randomly sampled from the static MNIST

dataset. The image resolution is  $64 \times 64$ , with each digit sized at  $28 \times 28$ . Each sequence contains 20 consecutive frames, where the first 10 frames serve as input and the last 10 frames as output. Both the training and test sets comprise 10,000 sequences.

**Implementation Details:** The GMG model is trained using an  $L1 + L2$  loss to simultaneously enhance the sharpness and smoothness of the generated frames. The specific model parameters, hyperparameters (such as batch size, learning rate, and training epochs), as well as the training hardware for each dataset, are detailed in Table I.

**Metrics:** We use common metrics to evaluate the predictive performance of the model, including MSE, MAE, RMSE, PSNR and SSIM. Specifically, for rainfall data, we also include the Critical Success Index (CSI) to assess forecast accuracy. A CSI value closer to 1 indicates higher prediction accuracy.

### B. Quantitative Evaluation

To analyze the performance of GMG compared to other SOTA models, we summarize the experimental results. Tables II, III, IV, and V present these quantitative results. Numbers highlighted in **Red Bold** indicate the best performance for the corresponding metric, while numbers marked with a Blue Underlined represent the second-best performance. In this study, we select deterministic models for comparison, including CNN, RNN, CNN-RNN, and ViT-based models. The selected models also include mainstream SOTA models such as SimVP and its variants, SwinLSTM, and WaST.

Table II presents the performance of baseline models and GMG on the CIKM2017 and Shanghai2020 datasets. GMG achieves leading performance across all metrics. Compared to the best-performing baseline models, GMG reduces the MSE by 8% on CIKM2017 and 4.1% on Shanghai2020. Additionally, SSIM improves by 0.0107 on CIKM2017 and 0.0012 on Shanghai2020. Notably, RNN-based models (e.g., MIM, MotionRNN, PredRNN-V2) tend to perform better in these two rainfall datasets. This may be attributed to the superior temporal modeling capability, spatial information capture, and effective long-term dependency modeling of recurrent neural networks.

Table III compares the performance of different models on the TaxiBJ dataset. Compared to the current best model, WaST, GMG achieves a new SOTA in MAE, SSIM, and PSNR. Compared to the baseline model MotionRNN, GMG reduces MSE by 20.63% and lowers MAE by approximately 7.9%.

Tables IV and V present the experimental results on the WeatherBench and Moving MNIST datasets, respectively, where GMG achieves comprehensive superiority across all evaluation metrics. With minor modifications, GMG, as an RNN-based model, outperforms the currently popular CNN and ViT models across different tasks. This provides a new perspective on utilizing recurrent neural networks for complex video prediction tasks in the future.

### C. Qualitative Evaluation

To further analyze the model’s performance in rainfall prediction, we visualize the results (Fig. 4). In the green-boxed

region, both ConvLSTM and TAU exhibit varying degrees of false alarms, while GMG accurately predicts rainfall in this area. Additionally, in the red-boxed region, neither ConvLSTM nor TAU detects the rainfall, but GMG successfully captures the development of rainfall from absence to presence. This highlights the significant contributions of the Global Focus and Motion Guided modules in improving prediction performance.

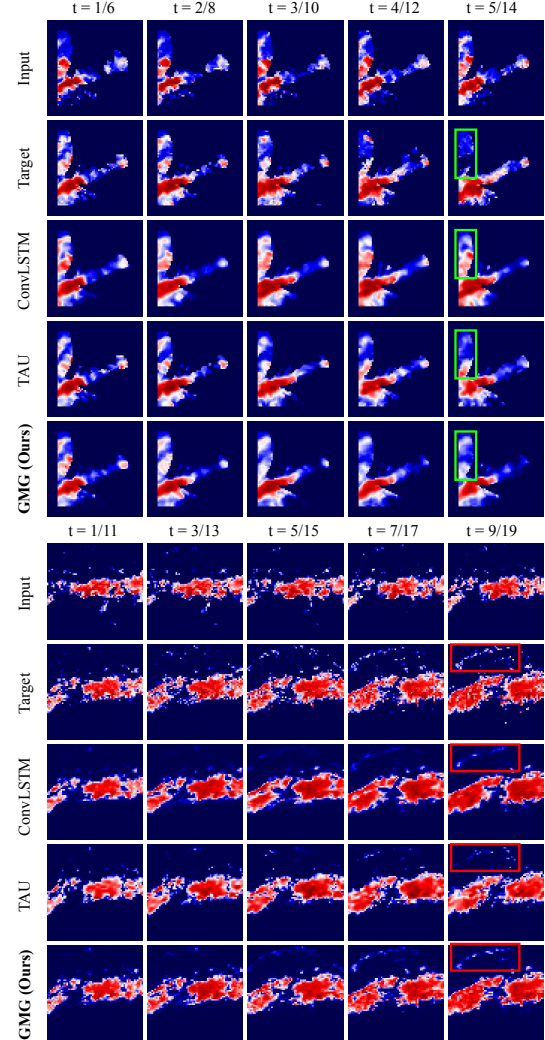


Fig. 4. Visualizations on CIKM2017 (upper) and Shanghai2020 (lower). The time labeled in the figure represents the input data time/predicted time.

Fig. 5 presents the experimental results on Taxibj, comparing the outcomes of TAU and WaST. In the main regions where errors occur (marked by green and red boxes), GMG consistently maintains the lowest error. This further demonstrates the effectiveness of the Global Focus Model in accurately capturing long-range dependencies.

Fig. 6 presents the visualization results for WeatherBench and Moving MNIST. We highlight the main error-prone regions in WeatherBench, and for better observation, all errors are magnified tenfold. GMG achieves the smallest error among all models. Although the variations in this dataset are relatively slower compared to rainfall data, the combined effect of the

TABLE I  
EXPERIMENTAL SETTINGS FOR DIFFERENT DATASETS.

Dataset	Patch / Batch size	Resolution	Model Type	Task	Epochs	Learning Rate	Att Hidden	GPU
CIKM2017	4/16	(1×64×64)	GMG-L	5 → 10	100	0.0003	32	1 * RTX4060Ti
Shanghai2020	4/16	(1×64×64)	GMG-L	10 → 10	200	0.0003	32	1 * RTX4060Ti
Taxibj	2/16	(2×32×32)	GMG-m	4 → 4	200	0.0003	64	1 * RTX4060Ti
WeatherBench	2/16	(1×32×64)	GMG-s	12 → 12	100	0.0003	64	4 * TESLA V100
Moving MNIST	4/16	(1×64×64)	GMG-L	10 → 10	600	0.0003	32	1 * TESLA V100

TABLE II  
QUANTITATIVE RESULTS ON CIKM2017 AND SHANGHAI2020 DATASETS.

Dataset	Model	Params	MSE (↓)	MAE (↓)	SSIM (↑)	CSI30 (↑)	CSI40 (↑)	CSI50 (↑)
CIKM2017	ConvLSTM (NeurIPS'2015) [23]	15.1M	28.8162	161.242	0.7359	0.7757	0.6590	0.5367
	PredRNN (NeurIPS'2017) [4]	23.8M	28.8126	159.404	0.7303	0.7803	0.6690	0.5471
	PredRNN++ (ICML'2018) [5]	38.6M	28.0987	159.258	0.7362	0.7775	0.6684	0.5533
	MIM (CVPR'2019) [6]	38.04M	<a href="#">27.2072</a>	<a href="#">154.269</a>	0.7388	0.7828	0.6725	<a href="#">0.5587</a>
	PyDNet (CVPR'2020) [15]	3.1M	28.9757	161.143	0.7393	0.7809	0.6654	0.5489
	MotionRNN (CVPR'2021) [7]	26.9M	27.2091	155.827	<a href="#">0.7406</a>	<a href="#">0.7867</a>	<a href="#">0.6762</a>	0.5510
	MAU (NeurIPS'2021) [21]	4.48M	30.9094	167.361	0.7234	0.7731	0.6584	0.5459
	PredRNN-V2 (TPAMI'2022) [8]	23.9M	28.0085	161.508	0.7374	0.7857	0.6640	0.5362
	SimVP-gSTA (CVPR'2022) [11]	4.82M	31.3121	166.261	0.7195	0.7731	0.6594	0.5416
	SimVP-ViT (NeurIPS'2023) [17]	39.6M	27.8803	157.478	0.7358	0.7835	0.6669	0.5483
	Swin-LSTM (ICCV'2023) [16]	20.19M	27.9612	158.899	0.7405	0.7826	0.6652	0.5532
	TAU (CVPR'2023) [12]	38.4M	30.5827	161.948	0.7277	0.7779	0.6601	0.5370
	WaST (AAAI'2024) [30]	28.18M	30.3074	165.804	0.7309	0.7773	0.6534	0.5174
	<b>GMG (Ours)</b>	31.44M	<b>25.0215</b>	<b>149.493</b>	<b>0.7513</b>	<b>0.7885</b>	<b>0.6812</b>	<b>0.5682</b>
Shanghai2020	ConvLSTM (NeurIPS'2015) [23]	15.1M	5.0219	39.236	0.9162	0.4321	0.4046	0.3584
	PredRNN (NeurIPS'2017) [4]	23.8M	4.3347	<b>34.297</b>	<a href="#">0.9288</a>	<a href="#">0.4707</a>	<a href="#">0.4451</a>	<a href="#">0.3992</a>
	PredRNN++ (ICML'2018) [5]	38.6M	4.7445	39.416	0.9190	0.4419	0.4100	0.3605
	MIM (CVPR'2019) [6]	38.04M	6.3924	44.986	0.8997	0.3910	0.3595	0.3131
	PyDNet (CVPR'2020) [15]	3.1M	7.6126	50.155	0.8846	0.3508	0.3124	0.2663
	MotionRNN (CVPR'2021) [7]	26.9M	4.5867	37.871	0.9221	0.4457	0.4183	0.3708
	MAU (NeurIPS'2021) [21]	4.48M	7.3441	50.766	0.8853	0.3485	0.3098	0.2599
	PredRNN-V2 (TPAMI'2022) [8]	23.9M	<a href="#">4.2050</a>	<a href="#">35.015</a>	0.9270	0.4543	0.4272	0.3815
	SimVP-gSTA (CVPR'2022) [11]	4.82M	8.0889	45.846	0.8908	0.3649	0.3406	0.2991
	SimVP-ViT (NeurIPS'2023) [17]	39.6M	9.9074	52.900	0.8718	0.3272	0.3053	0.2667
	Swin-LSTM (ICCV'2023) [16]	20.19M	6.7183	46.025	0.8957	0.3714	0.3371	0.2902
	TAU (CVPR'2023) [12]	38.4M	8.2874	47.315	0.8886	0.3630	0.3421	0.3000
	WaST (AAAI'2024) [30]	28.18M	6.1937	42.387	0.9063	0.3908	0.3545	0.3042
	<b>GMG (Ours)</b>	31.44M	<b>4.0308</b>	35.771	<b>0.9300</b>	<b>0.4741</b>	<b>0.4487</b>	<b>0.4002</b>

Global Focus Module and Motion Guided Module still enables the model to capture detailed temperature changes effectively.

For the Moving MNIST dataset, we provide visualizations comparing GMG with TAU. At the final prediction step (T=10), TAU produces a relatively blurry prediction of the digit "8" in the image, while GMG generates a much clearer result that is closer to the ground truth. Although the Motion Guided Module is primarily designed for non-rigid motion features, it also performs well in rigid motion prediction tasks. This demonstrates that GMG is versatile, adaptable to a wide range of scenarios, and has the potential to extend to more datasets.

From the above visualization results, we observe that GMG can adapt to various types of video prediction tasks, regardless of whether the predicted subject is a rigid or elastic body. Moreover, it achieves superior performance in terms

of prediction accuracy and object detail preservation. This demonstrates that GMG can serve as a general-purpose video prediction model, making it applicable to real-world complex video prediction tasks.

#### D. Ablation Study

To validate the contributions of GMG's individual components, we conduct ablation experiments on the CIKM2017 dataset, with results presented in Table VI. In addition to controlled experiments on key components—GFM, MGM, and SAM—we include comparisons with baseline models, PredRNN and MotionRNN. The results show that adding GFM, SAM, or MGM improves predictive performance over the baselines. Furthermore, compared to MotionGRU, model (A), which incorporates the MGM module to account for growth or dissipation processes, better captures rainfall data

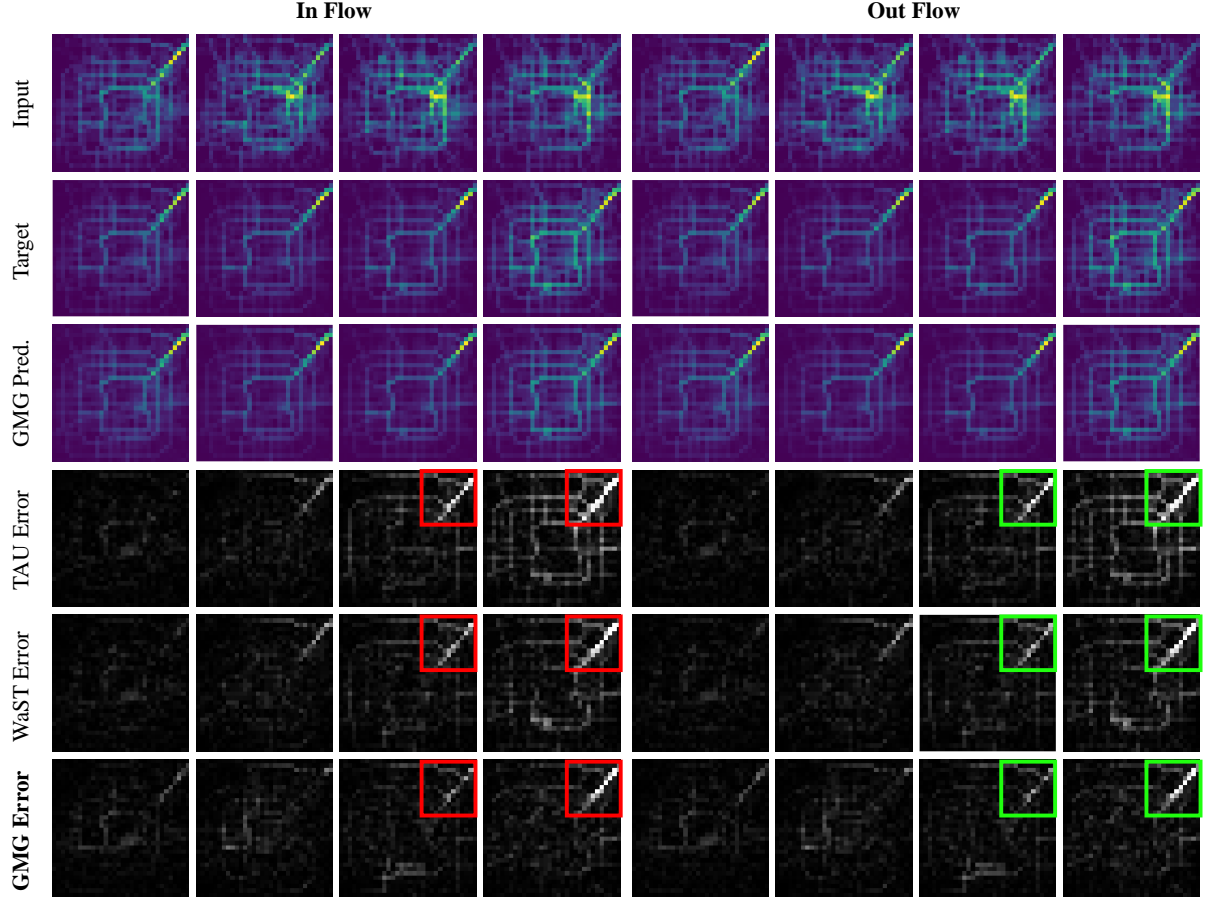


Fig. 5. Visualizations on Taxisb, Error =  $|\text{Prediction} - \text{Target}|$ , we amplify the error for better comparison.

TABLE III  
QUANTITATIVE RESULTS IN TAXIBJ DATASETS.

Model	MSE $\times 100$ ( $\downarrow$ )	MAE ( $\downarrow$ )	SSIM ( $\uparrow$ )	PSNR ( $\uparrow$ )
ConvLSTM [23]	40.0678	16.1892	0.9819	38.888
PredRNN [4]	35.0348	15.1302	0.9844	39.591
PredRNN++ [5]	41.8227	15.9766	0.9824	39.135
PyDNet [15]	40.1700	16.4790	0.9808	38.939
MotionRNN [7]	37.6517	16.0009	0.9825	39.001
MAU [21]	40.7206	15.6620	0.9822	39.353
PredRNN-V2 [8]	45.2737	16.6105	0.9807	38.713
SimVP-gSTA [11]	36.7385	15.3530	0.9832	39.509
Swin-LSTM [16]	35.9456	15.2276	0.9832	39.645
TAU [12]	35.1037	15.1745	0.9838	39.593
WasT [30]	<b>29.7753</b>	<b>14.7945</b>	<b>0.9846</b>	<b>39.777</b>
<b>GMG (Ours)</b>	<b>29.8812</b>	<b>14.7277</b>	<b>0.9850</b>	<b>39.831</b>

TABLE IV  
QUANTITATIVE RESULTS IN WEATHERBENCH DATASETS.

Model	MSE ( $\downarrow$ )	MAE ( $\downarrow$ )	RMSE ( $\downarrow$ )
ConvLSTM [23]	1.9703	0.8472	1.4036
PredRNN [4]	1.2881	0.7035	1.1349
MIM [6]	1.8480	0.8611	1.3594
MotionRNN [7]	<b>1.2607</b>	0.6813	<b>1.1228</b>
MAU [21]	1.4381	0.7548	1.1992
PredRNN-V2 [8]	1.8430	0.9029	1.3575
SimVP-gSTA [11]	1.5934	0.7654	1.2623
TAU [12]	1.4986	0.7375	1.2241
WaST [30]	1.3387	<b>0.6808</b>	1.1570
<b>GMG (Ours)</b>	<b>1.2341</b>	<b>0.6780</b>	<b>1.1109</b>

characteristics. By comparing Model (A), (B), and (C), MGM emerges as the most impactful component in enhancing baseline performance, followed by GFM, further validating the effectiveness of the proposed model design. Additionally, the lightweight version, GMG-s, achieves competitive results, offering a viable pathway for future lightweight modeling

efforts. We also provide the parameter count and training time for each model, offering a reference for practical model deployment.

## CONCLUSION

In this paper, we propose GMG, a video prediction model that integrates Global Vision and Motion Guidance to effectively capture spatial-temporal correlations. By introducing the



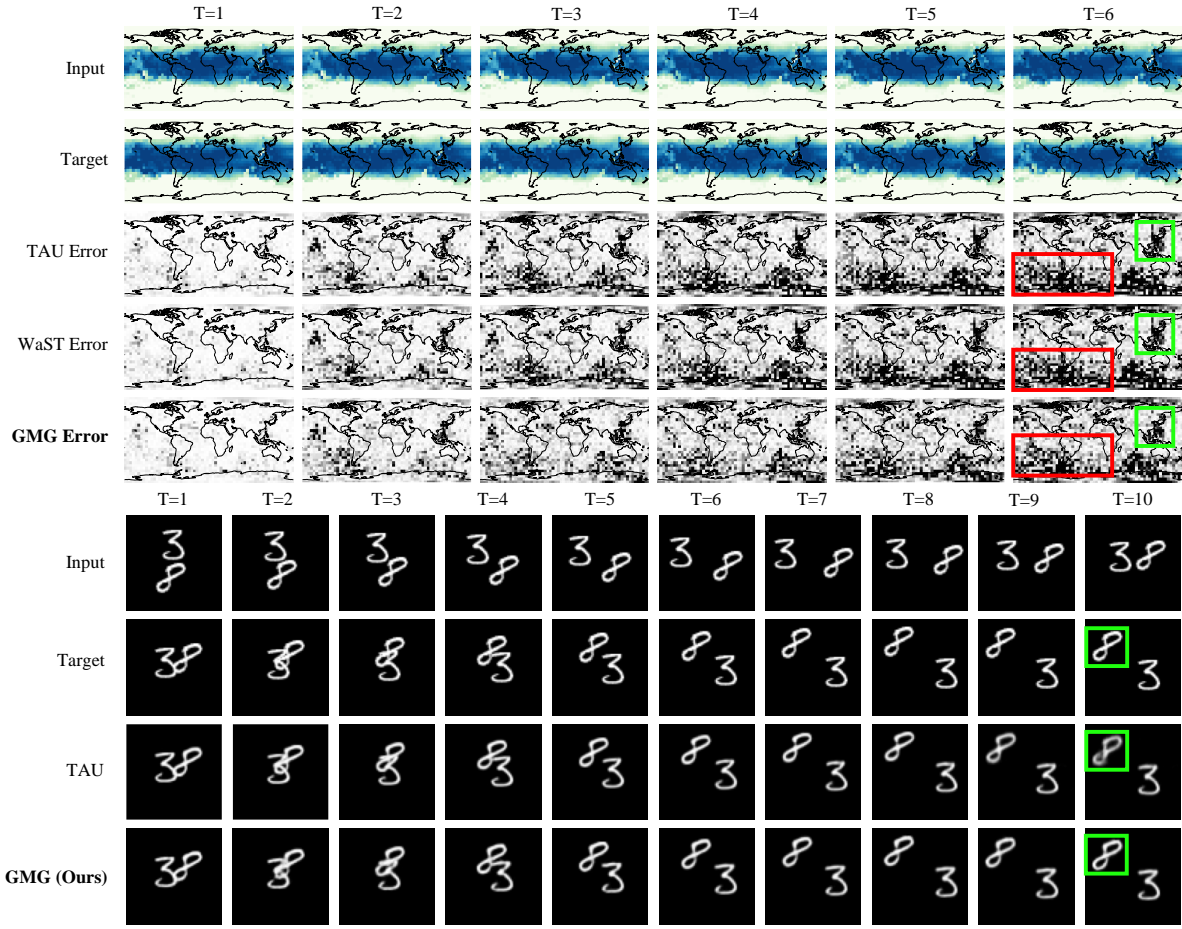


Fig. 6. Visualizations on WeatherBench (upper) and Moving MNIST datasets (lower) , Error =  $10 \times |\text{Prediction} - \text{Target}|$  , we amplify the error for better comparison.

TABLE V  
QUANTITATIVE RESULTS IN MOVING MNIST DATASETS.

Model	MSE ( $\downarrow$ )	MAE ( $\downarrow$ )	SSIM ( $\uparrow$ )	PSNR ( $\uparrow$ )
SimVP-gSTA [11]	22.5268	67.8671	0.9500	23.6783
SimVP-ViT [17]	26.4819	77.5663	0.9371	23.0279
SimVP-VAN [17]	20.5918	63.5674	0.9547	24.1267
SimVP-Poolformer [17]	25.5146	74.6528	0.9429	23.1193
Swin-LSTM [16]	<u>19.4554</u>	<u>61.2669</u>	<u>0.9571</u>	<u>24.3593</u>
TAU [12]	19.9112	62.1182	0.9562	24.3096
WasT [30]	22.0719	70.8779	0.9491	23.7451
<b>GMG (Ours)</b>	<b>19.0741</b>	<b>60.7413</b>	<b>0.9586</b>	<b>24.4606</b>

Global Focus Module (GFM) and Motion Guided Module (MGM), our model generalizes the non-rigid motion deformation process using a balancing factor  $\alpha$  and a decay factor  $\beta$ , enabling more precise predictions.

Extensive experiments on five benchmark datasets demonstrate that GMG significantly enhances prediction performance, surpassing existing mainstream methods while exhibiting strong generalization and application potential across different tasks.

Additionally, we provide model parameter sizes and training durations to facilitate real-world deployment. The lightweight version, GMG-s, also achieves competitive results, highlighting its potential for efficiency-critical applications. Overall, GMG outperforms existing CNN, RNN, and ViT-based models in video prediction, offering a novel solution for complex sequence forecasting.

## REFERENCES

- [1] Bi, Kaifeng, et al. "Accurate medium-range global weather forecasting with 3D neural networks." *Nature* 619.7970 (2023): 533-538.
- [2] Ravuri, Suman, et al. "Skilful precipitation nowcasting using deep generative models of radar." *Nature* 597.7878 (2021): 672-677.
- [3] Zhang, Junbo, Yu Zheng, and Dekang Qi. "Deep spatio-temporal residual networks for citywide crowd flows prediction." *Proceedings of the AAAI conference on artificial intelligence*. Vol. 31. No. 1. 2017.
- [4] Wang, Yunbo, et al. "Predrnn: Recurrent neural networks for predictive learning using spatiotemporal lstms." *Advances in neural information processing systems* 30 (2017).
- [5] Wang, Yunbo, et al. "Predrnn++: Towards a resolution of the deep-in-time dilemma in spatiotemporal predictive learning." *International conference on machine learning*. PMLR, 2018.
- [6] Wang, Yunbo, et al. "Memory in memory: A predictive neural network for learning higher-order non-stationarity from spatiotemporal dynam-

TABLE VI  
ABLATION STUDY RESULTS ON CIKM2017 DATASET.

Model index	GFM	SAM	MGM	Params	Traning Time (per epoch)	MSE ( $\downarrow$ )	MAE ( $\downarrow$ )	SSIM ( $\uparrow$ )
PredRNN	$\times$	$\times$	$\times$	23.8M	380s	28.8126	159.404	0.7303
MotionRNN	$\times$	$\times$	MotionGRU	26.9M	425s	27.2091	155.827	0.7406
(c)	$\times$	$\times$	$\checkmark$	26.9M	440s	26.4196	153.801	0.7462
(d)	$\times$	$\checkmark$	$\times$	31.4M	516s	26.9540	155.525	0.7444
(e)	$\checkmark$	$\times$	$\times$	30.4M	538s	26.7479	155.658	0.7448
(f)	$\checkmark$	$\checkmark$	$\times$	31.4M	627s	<a href="#">25.2383</a>	151.723	<b>0.7528</b>
<b>GMG-s (Ours)</b>	Simplified	$\checkmark$	$\checkmark$	29.2M	541s	25.3616	<a href="#">151.334</a>	0.7501
<b>GMG-m (Ours)</b>	$\checkmark$	$\times$	$\checkmark$	30.4M	455s	26.1861	152.472	0.7487
<b>GMG-L (Ours)</b>	$\checkmark$	$\checkmark$	$\checkmark$	31.44M	589s	<b>25.0215</b>	<b>149.493</b>	<a href="#">0.7513</a>

ics." Proceedings of the IEEE/CVF conference on computer vision and pattern recognition. 2019.

- [7] Wu, Haixu, et al. "MotionRNN: A flexible model for video prediction with spacetime-varying motions." Proceedings of the IEEE/CVF conference on computer vision and pattern recognition. 2021.
- [8] Wang, Yunbo, et al. "Predrnn: A recurrent neural network for spatiotemporal predictive learning." IEEE Transactions on Pattern Analysis and Machine Intelligence 45.2 (2022): 2208-2225.
- [9] Tang, Yujin, et al. "Vmrnn: Integrating vision mamba and lstm for efficient and accurate spatiotemporal forecasting." Proceedings of the IEEE/CVF Conference on Computer Vision and Pattern Recognition. 2024.
- [10] Xu, Ziru, et al. "PredCNN: Predictive Learning with Cascade Convolutions." IJCAI. 2018.
- [11] Gao, Zhangyang, et al. "Simvp: Simpler yet better video prediction." Proceedings of the IEEE/CVF conference on computer vision and pattern recognition. 2022.
- [12] Tan, Cheng, et al. "Temporal attention unit: Towards efficient spatiotemporal predictive learning." Proceedings of the IEEE/CVF Conference on Computer Vision and Pattern Recognition. 2023.
- [13] Wang, Yunbo, et al. "Eidetic 3D LSTM: A model for video prediction and beyond." International conference on learning representations. 2018.
- [14] Yu, Wei, et al. "Efficient and information-preserving future frame prediction and beyond." International Conference on Learning Representations. 2020.
- [15] Guen, Vincent Le, and Nicolas Thome. "Disentangling physical dynamics from unknown factors for unsupervised video prediction." Proceedings of the IEEE/CVF conference on computer vision and pattern recognition. 2020.
- [16] Tang, Song, et al. "Swinlstm: Improving spatiotemporal prediction accuracy using swin transformer and lstm." Proceedings of the IEEE/CVF International Conference on Computer Vision. 2023.
- [17] Tan, Cheng, et al. "Openstl: A comprehensive benchmark of spatiotemporal predictive learning." Advances in Neural Information Processing Systems 36 (2023): 69819-69831.
- [18] Tang, Yujin, et al. "PredFormer: Transformers Are Effective Spatial-Temporal Predictive Learners." arXiv preprint arXiv:2410.04733 (2024).
- [19] Dosovitskiy, Alexey. "An image is worth 16x16 words: Transformers for image recognition at scale." arXiv preprint arXiv:2010.11929 (2020).
- [20] Liu, Ze, et al. "Swin transformer: Hierarchical vision transformer using shifted windows." Proceedings of the IEEE/CVF international conference on computer vision. 2021.
- [21] Chang, Zheng, et al. "Mau: A motion-aware unit for video prediction and beyond." Advances in Neural Information Processing Systems 34 (2021): 26950-26962.
- [22] Zhong, Yiqi, et al. "Mmvp: Motion-matrix-based video prediction." Proceedings of the IEEE/CVF International Conference on Computer Vision. 2023.
- [23] Shi, Xingjian, et al. "Convolutional LSTM network: A machine learning approach for precipitation nowcasting." Advances in neural information processing systems 28 (2015).
- [24] Lin, Zhihui, et al. "Self-attention convlstm for spatiotemporal prediction." Proceedings of the AAAI conference on artificial intelligence. Vol. 34. No. 07. 2020.
- [25] Dai, Jifeng, et al. "Deformable convolutional networks." Proceedings of the IEEE international conference on computer vision. 2017.
- [26] Yao, Yichen, and Zhongjie Li. "CIKM AnalytiCup 2017: short-term precipitation forecasting based on radar reflectivity images." Proceedings of the Conference on Information and Knowledge Management, Short-Term Quantitative Precipitation Forecasting Challenge, Singapore. 2017.
- [27] Leiming Ma, et al. Shanghai-2020 Dataset. zenodo, October 26, 2022, doi:10.5281/zenodo.7251972.
- [28] Zhang, Junbo, Yu Zheng, and Dekang Qi. "Deep spatio-temporal residual networks for citywide crowd flows prediction." Proceedings of the AAAI conference on artificial intelligence. Vol. 31. No. 1. 2017.
- [29] Rasp, Stephan, et al. "WeatherBench: a benchmark data set for data-driven weather forecasting." Journal of Advances in Modeling Earth Systems 12.11 (2020): e2020MS002203.
- [30] Nie, Xuesong, et al. "Wavelet-Driven Spatiotemporal Predictive Learning: Bridging Frequency and Time Variations." Proceedings of the AAAI Conference on Artificial Intelligence. Vol. 38. No. 5. 2024.
- [31] Srivastava, Nitish, Elman Mansimov, and Ruslan Salakhudinov. "Unsupervised learning of video representations using lstms." International conference on machine learning. PMLR, 2015.